ACS APPLIED NANO MATERIALS

www.acsanm.org Article

Use of Machine Learning with Temporal Photoluminescence Signals from CdTe Quantum Dots for Temperature Measurement in Microfluidic Devices

Charles Lewis, James W. Erikson, Derek A. Sanchez, C. Emma McClure, Gregory P. Nordin, Troy R. Munro, and John S. Colton*

Cite This: *ACS Appl. Nano Mater.* 2020, 3, 4045−4053 Read Online

ACCESS | Metrics & More | Article Recommendations

ABSTRACT: Because of the vital role of temperature in many biological processes studied in microfluidic devices, there is a need to develop improved temperature sensors and data analysis algorithms. The photoluminescence (PL) of nanocrystals (quantum dots) has been successfully used in microfluidic temperature devices, but the accuracy of the reconstructed temperature has been limited to about 1 K over a temperature range of tens of degrees. A machine learning algorithm consisting of a fully connected network of seven layers with decreasing numbers of nodes was developed and applied to a combination of normalized spectral and time-resolved PL data of CdTe quantum dot emission in a microfluidic device. The data used by the algorithm were collected over two temperature ranges: 10−300 K and 298−319 K. The accuracy of each neural network was assessed via a mean absolute error of a holdout set of data. For the low-temperature regime, the accuracy was 7.7 K, or 0.4 K when the holdout set is restricted to temperatures above 100 K. For the high-temperature regime, the accuracy was 0.1 K. This method provides demonstrates a potential machine learning approach to accurately sense temperature in microfluidic (and potentially nanofluidic) devices when the data analysis is based on normalized PL data when it is stable over time.

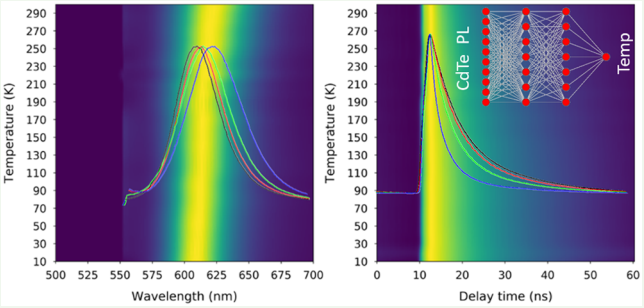

KEYWORDS: *photoluminescence, machine learning, thermometry, quantum dots, fluorescent lifetimes*

INTRODUCTION

Accurate temperature sensing at the micro- and nanoscale is necessary for a broad range of biologically relevant processes including organ-on-chip operation,[1] hypo- and hyperthermia,[2,3] biomolecular kinetics,[4] activation of temperature-sensitive mutations,[5] cryopreservation,[6] and DNA analysis such as melt curve analysis.[7] Microfluidic analysis of these biological processes has the added benefits of reduced sample and reagent use, parallelized analysis of multiple samples, and full automation of the analysis process. However, the number of temperature measurement methods that can be integrated into a microfluidic chip with the desired accuracy and spatial resolution is limited. As an example, in DNA melt curve analysis, a single nucleotide polymorphism is predicted to cause a difference in unwinding (i.e., "melting") temperature as small as 0.1 °C.[8] Existing sensors and data analysis algorithms cannot detect changes this small in a microfluidic device at the necessary temperature ranges, and so a new approach to temperature measurement should be investigated.

The requirements for a biothermal sensor are limiting[9,10] because the sensor has to meet some of the following requirements: biocompatibility, small probe size (nanoscale), rapid sensor response, and the ability to provide spatial[11] information about temperature. Typical biothermal sensing devices used in microfluidic devices include[10] IR and Raman thermography, thermocouples and platinum RTDs, liquid crystals, nano and bulk diamonds, and fluorescent dyes, proteins, and quantum dots,[12] with ref 13 providing an excellent review of shortcomings of the various sensors. In addition to the inherent uncertainties in the sensor, the data analysis algorithm (i.e., functional fitting to relate the sensor output to temperature) can introduce additional error. In a previous work,[14] we demonstrated that improved data analysis of nanocrystals (quantum dot, QD) fluorescence by machine learning improved the temperature prediction accuracy from

Received: January 8, 2020
Accepted: April 9, 2020
Published: April 9, 2020

https://dx.doi.org/10.1021/acsanm.0c00065
ACS Appl. Nano Mater. 2020, 3, 4045−4053

±1.0 to ±0.3 K over a range of 300−312 K. To accomplish this, several spectral features of QDs such as the absolute intensity of the fluorescent peak, the wavelength of peak emission, and the normalized intensity of the fluorescent spectra at several spectral bands were used as inputs to a neural network. The network was then trained to relate the spectral features to the temperatures measured with a calibrated platinum RTD. We have also achieved accuracies near ±0.6 K at times as short as 10 ns[15] using a stroboscopic technique. These approaches required the use of absolute values of peak intensity, so the accuracy of the approach was only applicable to that particular application. A more generalized approach is needed, particularly one that can be applied over a larger range of temperatures for biothermal sensing in microfluidic and nanofluidic devices. As an example application where improved thermal sensing could be used in microfluidic devices, there is evidence that changes as small as ±0.2 K can perturb biological processes and proteins in some cells, which is of interest for radio-frequency radiation interactions with human cells during cell phone use.[16]

Previously, the focus of machine learning via neural networks for thermal application has historically been on image recognition in thermal images.[17−19] A limited number of studies have used feed forward or convolution neural networks to predict temperature based on another signal. These include measuring atmospheric temperatures as a function of altitude,[20] determining temperature during combustion,[21] hyperspectral imaging trained on temperature at a single point,[22] and determining temperature distributions based on time-of-flight of ultrasound through tissue.[23] Based on these few instances with temperature and other sensors benefiting from machine learning use,[24] there is the potential to improve temperature sensing in biological system through the use of neural networks to interpret temperature sensitive signals.

The present study details the results of CdTe quantum dot fluorescence thermometry by means of an improved neural network. Fluorescent spectra and fluorescent lifetime data were acquired from a 3D printed microfluidic device over a temperature range from cryogenic (10 K) to several degrees above human physiological temperature[25] (319 K). The uniqueness of the approach is the use of normalized photoluminescence (PL) spectra data and time-resolved PL data instead of the total fluorescent intensity. Because of the nanoscopic size of fluorescent materials used, the results of this research present a data analysis method that can provide improved accuracy in measuring thermal transport at small scales.

EXPERIMENTAL METHODS

A microfluidic device was created to hold the CdTe quantum dots (Figure 1, PlasmaChem, λ_{max} = 650 nm) in place. This device was designed by using an open source CAD software (OpenSCAD) and printed on an Asiga 3D printer (Asiga Pico Plus 27, Asiga) with PR48 resin (Autodesk, Inc.). The Asiga was used because it has a 27 μm x−y resolution and a 10 μm z resolution[27] that was sufficient for the channel dimensions of the microfluidic device. The printed device was 12 mm × 12 mm × 4 mm with two parallel 1 mm × 1 mm channels for housing the quantum dots and a heating material. The PR48 resin was impregnated with CdTe quantum dots via sonication, injected into the device, and cured in place through an optical process (Figure 1). Previous work showed that this process does not affect the quantum dots' fluorescent thermal properties.[28] The device also had other channels, one of which is to get a thermocouple (TC, Type K, OMEGA Engineering) as close as possible to the embedded CdTe

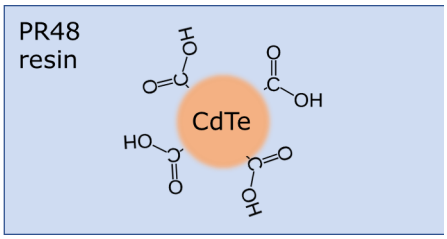

Figure 1. Schematic of COOH-functionalized CdTe nanoparticle inside open source PR48 resin. QDs were purchased as a powder from PlasmaChem and mixed into PR48 resin[26] as described in the text. Some of the key compounds in PR48 resin include Genomer 1122, Ebecryl 8210, and Sartomer SR 494.

quantum dots during the high-temperature measurements. The heating material was selected to be galinstan, a gallium-based liquid metal. This metal has a low enough viscosity to fill the channel and a high enough resistivity to provide heating when a current is passed through. Copper wires were placed in the external openings of the heating channel, and the channel was sealed off to protect the galinstan from oxidation. These copper wires were the access points for the DC power source used for the heating (BK Precision 1696). A schematic of the microfluidic device is shown in Figure 2b.

Photoluminescence (PL) spectral data and time-resolved PL data were taken using the optical setup shown in Figure 2a for temperatures between 10 and 319 K in two regimes: a low-temperature regime from 10 to 300 K in increments of 10 K and a high-temperature regime from 298 to 319 K in increments of 1 K. The CdTe quantum dot samples were sealed into PR48 resin chips and brought to the desired temperature points via (for low temperatures) a commercial cryostat or (for high temperatures) a custom PID controller which measures temperature with a thermocouple and drives a galinstan heating element embedded into the PR48 chip. We used different—but very similar—QDs for the low- and high-temperature regimes, each encapsulated in their own resin chip; the galinstan element was only present in the high-temperature regime chip. Representative PL spectra and time-resolved PL data are shown in Figure 3. Both wavelength and delay time curves display changes with temperature; therefore, optical data calibrated for temperature can be used to create an optical temperature probe.

The time-resolved PL was measured by using the technique of time-correlated single photon counting (TCSPC).[29] TCSPC involves measuring the time delay between PL excitation and PL emission. A timing module starts when it receives a trigger from a laser pulse and stops upon the detection of a photon from PL. This measurement is repeated many times, and the time values obtained are used to create a histogram. As per Figure 3b, the histogram shows a rise in photons incident on the detector as the laser pulse turns on and a decay in photons after the laser pulse shuts off. If the time scale of the decay approaches the time limitations of the system, then this measured data is not immediately representative of the sample's actual PL lifetime decay; instead, an instrument response function (IRF) must be obtained, and the measured TCSPC data will be the convolution of the IRF with the actual TRPL. In such cases the standard method of characterizing the decay is to assume a functional form for the actual decay using one or more parameters and then do an iterative reconvolution fit where the difference between the measured data and the convolution is minimized as the parameters are varied.[30]

However, this type of reconvolution fit requires knowing the precise functional form of the decay. In the simplest cases the optical decay may be a single exponential with a characteristic decay time describing the process. In more complicated situations, multiple discrete decay times can exist where each decay may have its own amplitude, or there could be a continuum of decay times that exist.[31] By doing convolution fits to our TCSPC data, we have found the CdTe quantum dots have at least two separate decay mechanisms, and possibly more, requiring several parameters to accurately model. The increased number of fitting parameters leads to large

https://dx.doi.org/10.1021/acsanm.0c00065
ACS Appl. Nano Mater. 2020, 3, 4045−4053

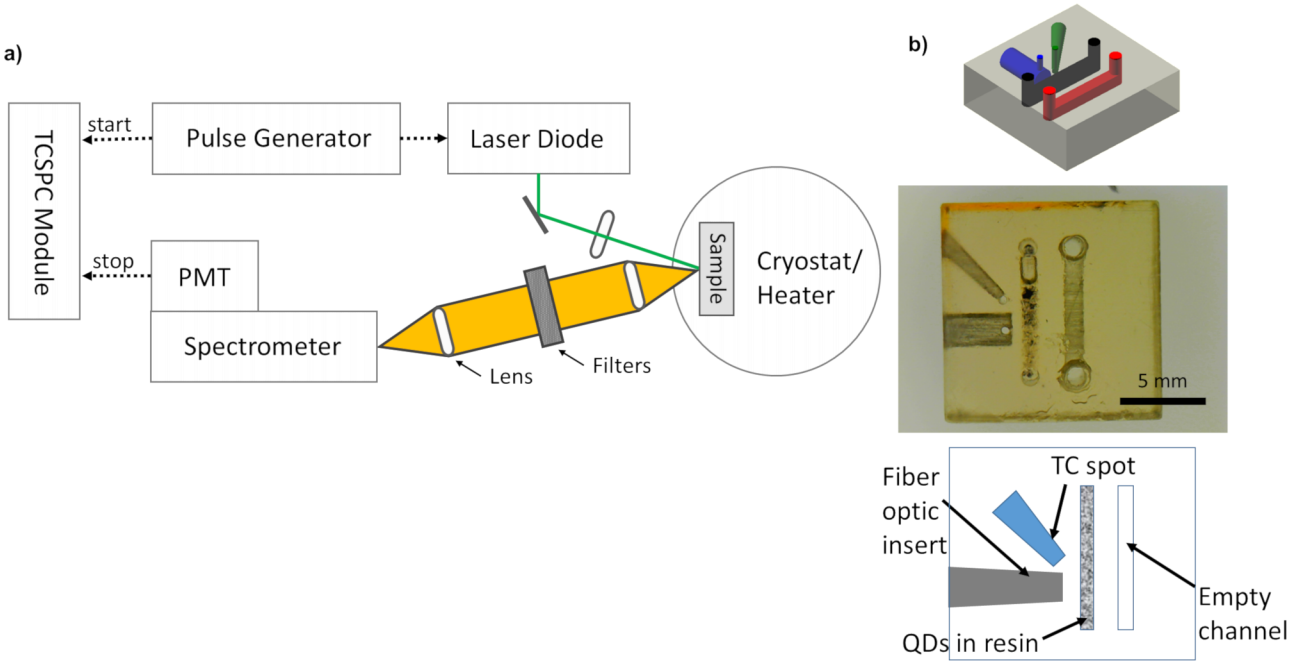

Figure 2. Optical experimental setup (a). The laser diode excites photoluminescence (PL) from the sample, which is placed in a cryostat or on a heating stage. The PL is collected and focused onto a spectrometer. For spectral scans the spectrometer analyzes the PL for wavelength dependence using a photomultiplier tube (PMT) detector or CCD detector (not shown). For time-resolved PL, the laser is controlled by a pulse generator which also sends the start signal to the TCSPC module, the spectrometer is set to the peak wavelength, and the PMT signal triggers the TCSPC module to stop. Microfluidic samples (b). CAD model sent to printer[27] and PR48-resin printed device with CdTe impregnated PR48 resin filling channels. Empty channels for the thermocouple (TC) and heating (galinstan) are shown.

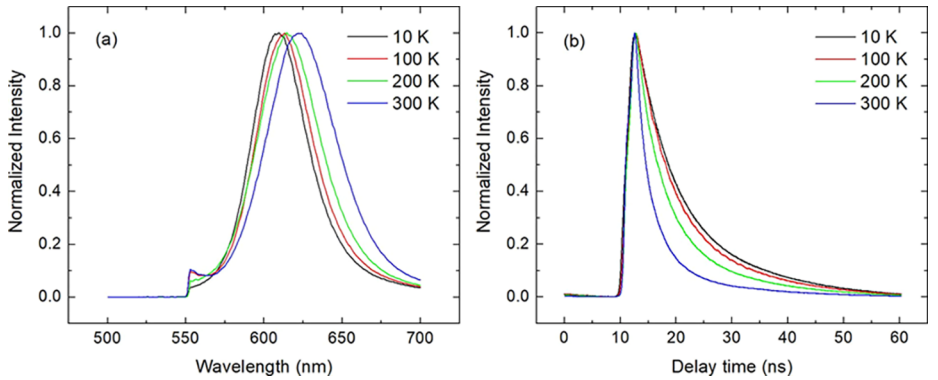

Figure 3. Representative normalized data from 10 to 300 K. (a) Spectral data (wavelength-resolved photoluminescence). (b) Time-resolved photoluminescence obtained via time-correlated single photon counting (TCSPC).

uncertainties in their values: a wide range of parameter values can lead to fits with approximately the same errors.[32] Therefore, in theory the PL lifetimes could be characterized as a function of temperature, and that function could be used to predict temperatures given newly measured time-resolved PL, but in practice that method proved extremely unreliable. This motivates our approach of using the measured TCSPC data itself, without any sort of decay model or reconvolution fit, as an input to a machine learning model. Instrument response function-less fitting of the data by Kalman filter has also been done with some success,[33] but the use of neural networks is expected to provide improved results.

To take the optical data, a 520 nm laser (Thorlabs TCLDM9 diode laser, 500 MHz bandwidth) is focused onto the sample (see Figure 2a). The laser is modulated via an external pulse generator (Agilent 81110A) to provide 5 ns pulses every 60 ns and has an average power of 0.2 mW. The PL emission is collimated and filtered with a 550 nm long pass filter to remove stray laser light. The filter cuts off wavelengths below 550 nm in Figure 3a, producing a sharp shoulder. Because the PL emission is roughly 10 times weaker for high temperatures compared to low temperatures, the shoulder is more pronounced in the normalized spectra plotted. The filtered emission is then focused onto a spectrometer (JY Horiba Triax 550). For each temperature, the sample's PL spectrum is first measured; we used a cooled photomultiplier tube (PMT) detector with photon counter for the low-temperature regime (Hamamatsu R3896 PMT; Stanford Research Systems SR400 photon counter) and a cooled CCD detector for the high-temperature regime (JY Horiba Synapse 354010). Then, for the TCSPC measurements, the spectrometer is set to the peak of the spectrum with a spectral bandwidth of 0.3 nm. The time-resolved PL in both regimes is detected with the PMT, with timing provided by a Picoquant TimeHarp 260 pico TCSPC board.

To ensure the photostability of the PL, spectral data were collected for three consecutive days under 100 mW illumination, with multiple tests performed on the third day. The results are shown in Figure 4 and demonstrate that the CdTe emission is reasonably stable over multiple days. Additionally, each test in represented in Figure 4 lasted about 50 min where the laser was continuously irradiating the QDs.

https://dx.doi.org/10.1021/acsanm.0c00065
ACS Appl. Nano Mater. 2020, 3, 4045−4053

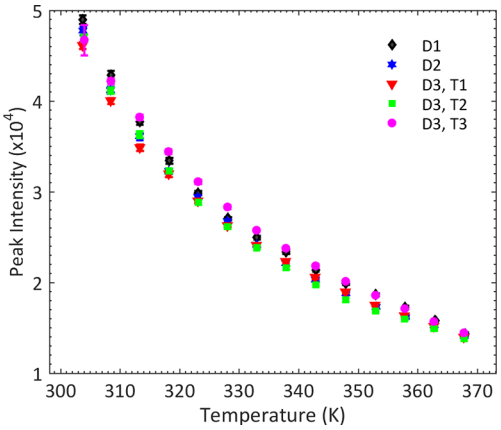

Figure 4. Peak intensity of CdTe dots embedded in a polymer matrix, showing stability of the PL signal over 3 days (D1−D3), and multiple tests on the same day (T1−T3).

This QD stability was also observed during our previous work with CdSe/ZnS QDs not in a polymer matrix.[34]

With regard to the TCSPC measurement, start triggers occur every 60 ns. An overall delay is present so the response to the laser pulse does not occur at zero time, as can be seen in Figure 3b. The PL is dimmed with neutral density (ND) filters to reach a rate of 450000 photons per second. The rate was selected so that PL photons are collected in fewer than 5% of the trigger periods to minimize the chance of two photons being collected by our optical system during a given trigger period—otherwise, the data would be skewed to shorter times as the second photon would go undetected.[35] Because the PL emission strength depends on temperature, the amount of added ND filtering required to achieve that rate also depends on temperature, typically ranging from ND0 (i.e., no added filter) for high temperatures to ND1 for low temperatures.

The spectral data and the TCSPC data were used jointly as the machine learning inputs.

Machine Learning Setup. The data for machine learning were preprocessed in two ways. First, we calculated the logarithm of our TCSPC data prior to inputting the data into the neural network. This is analogous to the case of a single-exponential decay fit where a researcher might take the log of a decay function and do a linear least-squares fit to the log data rather than doing an exponential decay least-squares fit on the raw data. Roughly speaking, taking the log first gives more weight to points on the decay at later times than they otherwise would have.

Second, even though the PL intensity correlates quite strongly with temperature, we used a (0, 1) min−max normalization[36] on each data set to deliberately cause that potential learning feature to be lost. This was done because the absolute intensity, while temperature dependent, is also heavily dependent on factors such as specific detectors, optical alignment, and geometry (i.e., solid angle collected), which will vary heavily from one laboratory to another. Machine learning results obtained with the normalization in place should therefore provide a more representative idea of what can be achieved with training data obtained in one laboratory and later optical measurements, i.e., the inputs for the trained machine learning model, being performed in a different place.

As mentioned above, the low-temperature regime contained data from 30 temperatures (from 10 to 300 K in steps of 10 K) and the high-temperature regime contained data from 22 temperatures (from 298 to 319 K in steps of 1 K). Details on the optical data files are provided in Table 1.

Three distinct sets of data were used in the machine learning process and are defined as follows. The *training set* refers to the set of data that was used to train the neural network. The *testing/validation set* refers to the set of data that was used to test the neural network during its development, for example, to guard against overfitting. The *holdout set* refers to the set of data that was withheld completely during the training process and used to establish the validity of the final neural network.

Table 1. Optical Data File Details

optical measurement	scan range	step size	no. of points
low-temperature spectrum	500−700 nm	1.000 nm	201
high-temperature spectrum	500−700 nm	1.041 nm	193
TCSPC	0−60.275 ns	0.025 ns	2412

Our basic machine learning methodology was to do the following for each of the two temperature regimes. We first withheld data from five randomly selected temperatures for later use. This is the holdout set. We then interpolated between the remaining temperatures to generate additional samples which were then used as the inputs to train the neural network. Interpolation is a form of data set augmentation, which is especially useful for smaller data sets when it is difficult or untimely to find or create new data and has been used in contexts such as the visualization of sinusoids, the classification of pen characters, and the classification of spoken Arabic words.[37] It is somewhat similar to image recognition machine learning routines which create new training images by performing rotations or reflections of the original images, zooming in and out, changing the color palette, and so forth.[38] After creating the interpolated files, we used a random 80/20 "training/testing split" to create the training set and the testing/validation set. The neural network was trained using only points from the training set. Hyperparameters were varied and tuned to obtain the best neural network (more details below). Finally, the mean absolute error of the holdout set was used to assess and report on the quality of the neural network.

The temperatures for the holdout set in the low-temperature regime were as follows: 70, 90, 120, 180, and 250 K. The interpolation was done in steps of 1 K using the remainder of the temperatures, creating data from 10 to 300 K. The final set of 291 pairs of normalized spectral and TCSPC data for the low-temperature regime, 10 to 300 K in steps of 1 K, which were used for machine learning training are plotted in Figure 5.

The temperatures for the holdout set in the high-temperature regime were as follows: 301, 305, 310, 313, and 316 K. The interpolation was done in steps of 0.1 K using the remainder of the temperatures, creating data from 298 to 319 K. The final set of 211 pairs of spectral and TCSPC data which were used for machine learning training are plotted in Figure 6.

Neural Network Optimization. We pursued various architectures for an artificial neural network to be able to accept optical spectral and TCSPC data and predict temperature. These include a convolutional neural network (CNN) with the spectral and TCSPC data feeding into separate branches (merging them together in a later layer), a CNN with the spectral and TCSPC data feeding in as a single input vector, a dense fully connected neural network (DNN) with the spectral and TCSPC data feeding in separately, a DNN using only the spectral data, a DNN using only the TCSPC data, and a DNN with the spectral and TCSPC data feeding in as a single vector. Within each of these architectures, we tested network parameters such as number of hidden layers and number of nodes per layer. We also tested k-fold cross validation (with $k = 5$) for the "input together" DNN as an alternative to the 80−20 training/testing split technique. These were all tested for the low-temperature regime; results are presented in Table 2.

The optimal architecture proved to be an "input together" DNN in which the spectral and TCSPC data were merged into a single vector of length 2613 as the input layer. Additional hyperparameters such as numbers of layers and nodes per layer, activation functions (relu, tanh, sigmoid, and linear), learning rate (multiple values), and optimizer (adam, adagrad, adadelta, and sgd) were tuned using standard practices.[39,40] Batch normalization was also explored as a hyperparameter. Principal component analysis using feature elimination was also investigated as a preprocessing technique to simplify the data and reduce unnecessary information; however, it was not used in the final machine learning model because none of the models performed better

https://dx.doi.org/10.1021/acsanm.0c00065
ACS Appl. Nano Mater. 2020, 3, 4045−4053

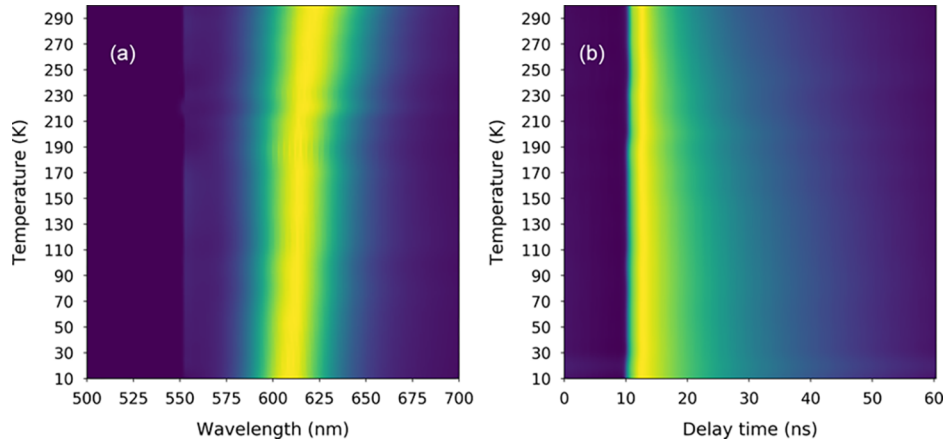

Figure 5. Complete set of training data with interpolations for the low-temperature regime. (a) Spectral data. (b) TCSPC data. Aside from the logarithm preprocessing step for the TCSPC data mentioned in the text, the plots shown in Figure 2 are horizontal slices of these images at 10, 100, 200, and 300 K.

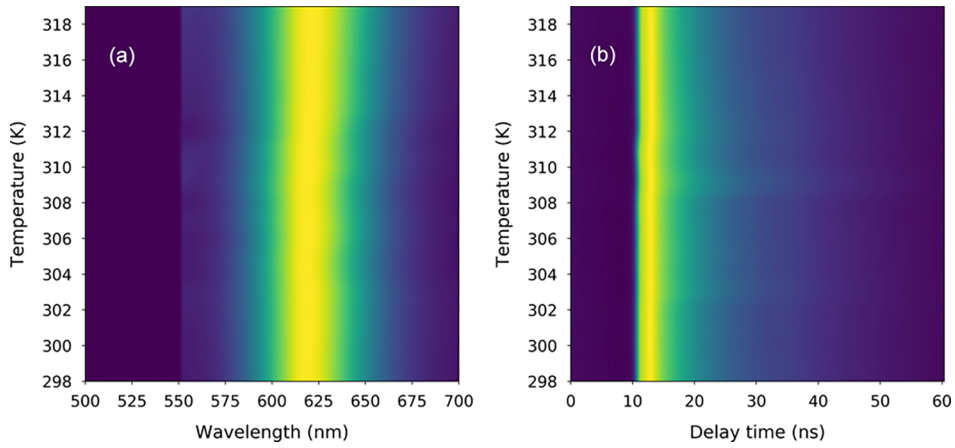

Figure 6. Complete set of training data with interpolations for the high-temperature regime: (a) spectral data; (b) TCSPC data.

Table 2. Results for Various Architectures in the Low-Temperature Regime

architecture	mean absolute error of holdout data set (in K)
two input CNN	13.6
input together CNN	9.9
two input DNN	8.4
spectra only DNN	9.2
TCSPC only DNN	11.3
input together DNN	7.7
DNN (*k*-fold cross validation, $k = 5$)	7.9

with the reduced dimensionality. The optimal network was obtained with ReLU activation functions, a learning rate of 0.001, the adam optimizer, no batch normalization, and a seven-layer DNN with decreasing numbers of nodes as follows: 512, 256, 128, 64, 32, 16, and 1. The output layer gives the temperature prediction for the given optical spectral and TCSPC data inputs.

The high-temperature regime neural network was created using the same architecture and hyperparameters as the low-temperature regime, albeit with an input vector length of 2605 due to the slightly different spectral data file size.

For all of our neural network training, we used the Keras API in Python with TensorFlow backend. The training used a mean-squared error loss function and proceeded for 6.000 epochs. Because of substantial loss function fluctuations during training—undoubtedly a result of a combination of factors such as choice of learning rate, loss function, and limited number of training samples[41]—we employed the "restore_best_weights = true" option to the EarlyStopping function to preserve the best neural network weights from epoch to epoch despite the fluctuations.[40] A plot of the loss function during the training process is shown in Figure 7, with the light gray values being the loss function at each epoch and the dark black values being the loss function for the current best weights. The loss function of the

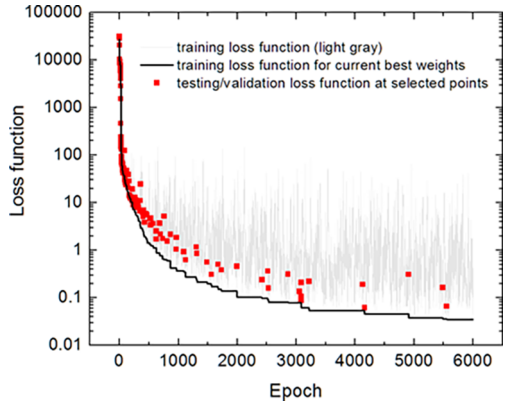

Figure 7. Plot of loss functions of training and testing sets during neural network training for the low-temperature regime.

https://dx.doi.org/10.1021/acsanm.0c00065
ACS Appl. Nano Mater. 2020, 3, 4045−4053

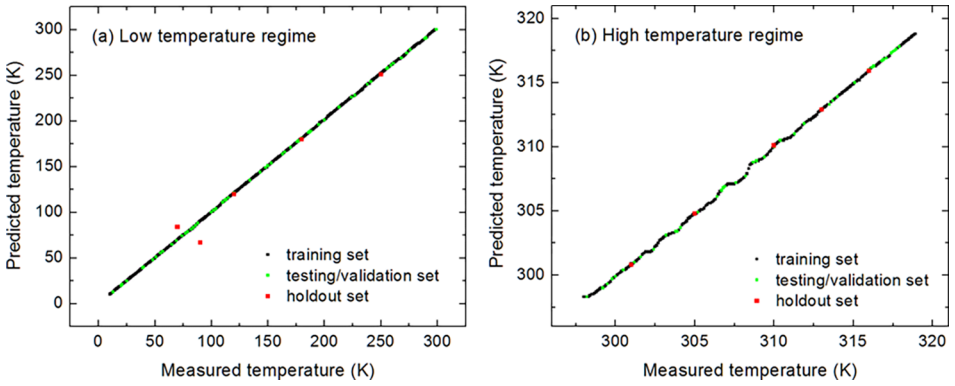

Figure 8. Performance of the neural networks on training, testing/validation, and holdout sets for (a) the low-temperature regime and (b) the high-temperature regime.

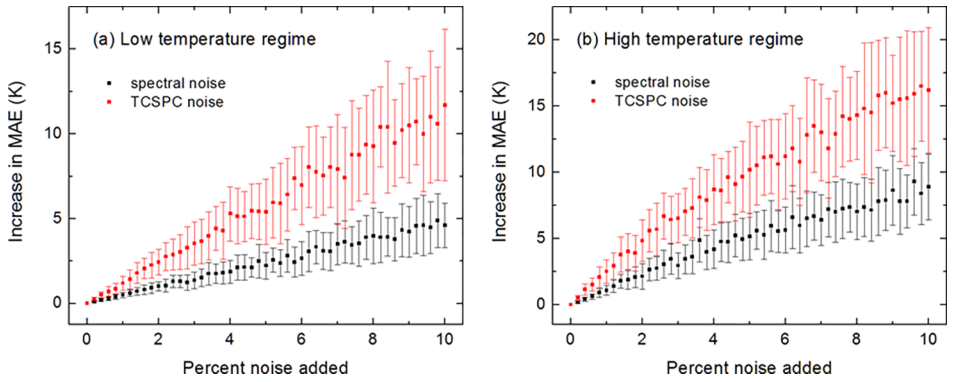

Figure 9. Performance of neural network predictions with noise artificially added to the optical data for (a) the low-temperature regime and (b) the high-temperature regime.

testing/validation set is displayed in red for selected points, namely, the points at which the best weights changed.

Neural Network Results. The performance of the neural networks is presented in Figure 8, where the predicted temperatures are plotted vs the actual measured temperatures. The line $y = x$ would indicate perfect predictions. Despite the wiggles apparent in the high-temperature regime, due to the magnified temperature scale, that regime is actually more accurate than the low-temperature regime. Within the low-temperature regime, it is all quite accurate except for two of the red points (holdout set) which are at 70 and 90 K and are discussed more below.

The reason for the large error at the holdout points of 70 and 90 K is likely due to two factors. First, as can be seen in the plots of Figure 3, the optical properties change less per unit temperature at low temperatures than they do at higher temperatures. Both spectral and TCSPC data change much more going from 200 to 300 K than they do going from 10 to 100 K. This is a result of how the semiconductor band gap shifts with temperature, mainly arising due to thermal expansion. As temperature increases, the atoms get farther and farther apart. This increase in lattice constant decreases the potential seen by the electrons in the material, which in turn reduces the size of the energy band gap (increasing the PL peak wavelength). The thermal expansion is nonlinear, with greater expansion per unit temperature at higher temperatures;[42] the corresponding temperature dependence of the band gap is often modeled with Varshni's.[43] As a second factor, because of time constraints and the wide range of temperatures involved in the low-temperature regime, we only took data every 10 K (and interpolated to 1 K) as compared with 1 K (interpolated to 0.1 K) for the high-temperature regime. While the neural network was still able to perform well for the training and the testing/validation sets even for temperatures below 100 K, these limitations for low temperatures were clearly manifest in the errors of the holdout set data of 70 and 90 K.

The holdout set results are summarized as follows. For the low-temperature regime, using all five holdout temperatures, the mean absolute error (MAE) was 7.7 K. For the low-temperature regime, restricting the holdout set to temperatures over 100 K only, the MAE was 0.4 K. For the high-temperature regime, the MAE of the holdout set was 0.1 K.

Neural Network Additional Testing. To investigate the performance of the neural networks further, we performed several types of additional testing. First, as was mentioned above, the PL is filtered with a 550 nm long pass filter, which creates abrupt shoulders in the spectra as can be seen in Figure 3. To determine the dependence of the neural networks on this particular type of optical filter, we artificially smoothed the PL spectral data at the location of the shoulders for the 10 holdout points and ran the smoothed data through the neural network again. Relative to the neural network predictions with the abrupt shoulders, the predictions for the smoothed shoulders changed by 5.0 K MAE and 1.2 K MAE for the low- and high-temperature regimes, respectively.

To test the effects of added noise on optical measurements, we artificially added random noise to the data from the holdout points and ran the noisy data through the neural network again. The noise was added just prior to the neural network input. The noise for a given "percent noise added" value was sampled from a uniform distribution between negative and positive values of the percentage added (as a percentage of the maximum value). This was done 40 times for each "percent noise added" value, and means and standard deviations of the MAE for the holdout points relative to the neural network predictions with no added noise were computed. The results are displayed in Figure 9. For both regimes, the neural networks were tolerant of noise to some degree, and they displayed a larger tolerance for noise added to the spectral data than noise added to the TCSPC data.

https://dx.doi.org/10.1021/acsanm.0c00065
ACS Appl. Nano Mater. 2020, 3, 4045−4053

However, some types of variations to the data are undoubtedly more pernicious than others. For example, using a different optical detector with a slightly different spectral response (e.g., CCD vs PMT) caused the predicted temperature in one example to shift by 7 K. Any shifts in the optical properties as a result of laser exposure or long-term changes to the QDs can cause substantial changes to the temperature predictions, depending on the amount of change and the temperature regime. For example, measurements done several months after the ones used to train the neural network displayed substantial changes to both spectral and TCSPC data presumably due to changes in QD composition and/or size and gave rise to meaningless predictions. Even measurements done in the same day at the same temperature (e.g., start of day vs end of day after having been illuminated by laser for several hours) could result in temperature predictions which differed by 5−10 K. Therefore, for real-world applications care should be taken to find QDs that are extremely stable against both short- and long-term changes, and these specific results should be considered only to be a proof of principle of our machine learning technique.

DISCUSSION

The holdout set results are summarized as follows. For the low-temperature regime (the 10−300 K range), by using all five holdout temperatures, the mean absolute error (MAE) was 7.7 K. For the low-temperature regime, restricting the holdout set to temperatures over 100 K only, the MAE was 0.4 K. For the high-temperature regime (the 298−319 K range), the MAE of the holdout set was 0.1 K. It is useful to compare these results to previous work[34] for PL behavior of QDs under different conditions, namely on- and off-chip. In ref 34, we investigated the temperature-dependent spectrum of CdSe−ZnS QDs that had been deposited onto a surface from a toluene solution, rather than being embedded in a polymer resin. Although the shape of the CdSe/ZnS spectrum is different than the CdTe QDs used in this study, the general spectral response to temperature changes is similar. The previous work used a very narrow temperature range (300−312 K) and obtained an accuracy of ±0.3 K through the use of a simply connected neural network trained on bands of the normalized intensity. By modification of the structure of the neural network to the one presented in this work and by incorporation of data on the lifetime of the PL, the error in the temperature reconstruction was reduced and the temperature range was increased.

When considering the limitations of applying our approach to luminescent materials, one has to consider how well the network would be able to reconstruct the temperature using nanoparticles that undergo structural changes such as perovskites.[44] The interpolation scheme could not be used around the transition temperature; instead, additional measurements near this temperature would be required, which warrants further study. However, machine learning techniques have been able to account for interactions with the fluorophore and the surrounding matrix going through a glass transition (Rhodamine B in glycerol).[15] The neural network was able to still capture the temperature behavior of the PL where the intensity decreased as temperature decreased (which is the inverse of what typically happens). They reasoned that the fluorophore interacting with the surrounding material resulted in electron transfer or thermal activation from a long-lived dark state. The neural network was able to incorporate this behavior in its model. An additional consideration is how the variation in nanoparticle size distribution between different batches of QD production will cause a slight variation in the PL spectra. To account for this variation and generalize the presented methods, we would propose that PL and lifetime measurements are taken at room temperature and compared to the normalized values presented in this work. The difference can then be considered as a bias to be applied at other temperatures, but this approach as well as investigations into the use of rare-earth-doped inorganic nanoparticles (NPs) with long lifetimes[45] (from 1 to 100 μs for Nd-based[46] and Eu[47]- or Er[46]-based NPs, respectively, to several milliseconds for Tb^{3+}[48,49] and some Yb NPs[45]) would require additional investigation as well.

As an example of the applicability of the proposed approach to biomedical sensing, there is a need to accurately measure the temperature during the melt curve analysis of DNA. The change in the temperature at which DNA strand unwinds (or "melts," T_m) for either a wild-type DNA sequence or a homozygous mutation varies depending on the number of SNPs (single nucleotide polymorphisms) and the length of the amplicon. This detection is limited by the absolute temperature accuracy of the real-time PCR device. This type of SNP (homozygous mutant vs wild type[7]) is important to detect because in several genetic conditions having two mutant alleles increases the severity of the disease. Heterogeneous mutant melt curves are easier to distinguish because they have a distinctive shape, while the homozygous and wild-type curves can look almost identical except for a slight change in T_m.[50] Because typical accuracies for fluorescent thermometry are near ±1 K,[10] they are incapable of seeing the slight change in melting temperature (0.2 K for Factor V Leiden G>A mutation[51]) observed with a homozygous mutant. However, the proposed work can obtain that level of accuracy.

CONCLUSION

A robust and reliable machine learning model for thermometry using nanoparticles (QDs) was obtained by using a combination of raw spectral and time-resolved PL data as the inputs. The inputs were normalized, so intensity was not present as a learning feature, to be representative of what may occur when using different experimental systems for the training samples and the later use of the model. Data augmentation vis interpolation was employed to increase the number of training samples by a factor of 10. The accuracy of each neural network was assessed via mean absolute error of a holdout set of data. For the low-temperature regime, the accuracy (mean absolute error of a holdout set) was 7.7 K, or 0.4 K when the holdout set was restricted to temperatures above 100 K. For the high-temperature regime, the accuracy was 0.1 K. The implementation of this method can impact nanoscale sensing accuracy and resolution of microfluidic, biothermal sensors and expand the number of temperature-sensitive analyses possible without having to calibrate each microfluidic device individually, although care needs to be taken in the selection of quantum dots to guard against short- and long-term changes to the optical emission.

AUTHOR INFORMATION

Corresponding Author

John S. Colton − *Department of Physics and Astronomy, Brigham Young University, Provo, Utah 84602, United States*; Email: john_colton@byu.edu

Authors

Charles Lewis − *Department of Physics and Astronomy, Brigham Young University, Provo, Utah 84602, United States*

https://dx.doi.org/10.1021/acsanm.0c00065
ACS Appl. Nano Mater. 2020, 3, 4045−4053

James W. Erikson − *Department of Physics and Astronomy, Brigham Young University, Provo, Utah 84602, United States*
Derek A. Sanchez − *Department of Mechanical Engineering, Brigham Young University, Provo, Utah 84602, United States*
C. Emma McClure − *Department of Physics and Astronomy, Brigham Young University, Provo, Utah 84602, United States*
Gregory P. Nordin − *Department of Electrical and Computer Engineering, Brigham Young University, Provo, Utah 84602, United States;* orcid.org/0000-0001-7241-5764
Troy R. Munro − *Department of Mechanical Engineering, Brigham Young University, Provo, Utah 84602, United States;* orcid.org/0000-0002-2557-4911

Complete contact information is available at: https://pubs.acs.org/10.1021/acsanm.0c00065

Notes

The authors declare no competing financial interest.

■ ACKNOWLEDGMENTS

We are grateful to the National Institutes of Health (1R15GM132868-01 and R15GM123405) for support of this work.

■ REFERENCES

(1) Zhang, Y. S.; Aleman, J.; Shin, S. R.; Kilic, T.; Kim, D.; Mousavi Shaegh, S. A.; Massa, S.; Riahi, R.; Chae, S.; Hu, N.; Avci, H.; Zhang, W.; Silvestri, A.; Nezhad, A. S.; Manbohi, A.; De Ferrari, F.; Polini, A.; Calzone, G.; Shaikh, N.; Alerasool, P.; Budina, E.; King, J.; Bhise, N.; Ribas, J.; Pourmand, A.; Skardal, A.; Shupe, T.; Bishop, C. E.; Dokmeci, M. R.; Atala, A.; Khademhosseini, A. Multisensor-Integrated Organs-on-Chips Platform for Automated and Continual in Situ Monitoring of Organoid Behaviors. *Proc. Natl. Acad. Sci. U. S. A.* **2017**, *114* (12), E2293−E2302.
(2) Huang, X.; El-Sayed, M. A. Gold Nanoparticles: Optical Properties and Implementations in Cancer Diagnosis and Photothermal Therapy. *Journal of Advanced Research* **2010**, *1* (1), 13−28.
(3) Wen, S.; Miao, X.; Fan, G.-C.; Xu, T.; Jiang, L.-P.; Wu, P.; Cai, C.; Zhu, J.-J. Aptamer-Conjugated Au Nanocage/SiO_2 Core−Shell Bifunctional Nanoprobes with High Stability and Biocompatibility for Cellular SERS Imaging and Near-Infrared Photothermal Therapy. *ACS Sens.* **2019**, *4* (2), 301−308.
(4) Yang, T.; Stavrakis, S.; Arosio, P.; deMello, A. A Temperature-Controlled Stopped-Flow Droplet-Based Microfluidic Reactor for Fast Biomolecular Kinetics. *Biophys. J.* **2018**, *114* (3), 586a.
(5) Tan, G.; Chen, M.; Foote, C.; Tan, C. Temperature-Sensitive Mutations Made Easy: Generating Conditional Mutations by Using Temperature-Sensitive Inteins That Function Within Different Temperature Ranges. *Genetics* **2009**, *183* (1), 13−22.
(6) Pegg, D. E. Principles of Cryopreservation. In *Cryopreservation and Freeze-Drying Protocols*; Day, J. G., Stacey, G. N., Eds.; Methods in Molecular Biology; Humana Press: Totowa, NJ, 2007; pp 39−57.
(7) Chen, T.; Jia, Y.; Dong, C.; Gao, J.; Mak, P.-I.; Martins, R. P. Sub-7-Second Genotyping of Single-Nucleotide Polymorphism by High-Resolution Melting Curve Analysis on a Thermal Digital Microfluidic Device. *Lab Chip* **2016**, *16* (4), 743−752.
(8) Reed, G. H.; Kent, J. O.; Wittwer, C. T. High-Resolution DNA Melting Analysis for Simple and Efficient Molecular Diagnostics. *Pharmacogenomics* **2007**, *8* (6), 597−608.
(9) Young, A. T.; Rivera, K. R.; Erb, P. D.; Daniele, M. A. Monitoring of Microphysiological Systems: Integrating Sensors and Real-Time Data Analysis toward Autonomous Decision-Making. *ACS Sens.* **2019**, *4* (6), 1454−1464.
(10) Kucsko, G.; Maurer, P.; Yao, N.; Kubo, M.; Noh, H.; Lo, P.; Park, H.; Lukin, M. Nanometre-Scale Thermometry in a Living Cell. *Nature* **2013**, *500* (7460), 54−58.
(11) Fu, G.; Zhu, Y.; Wang, W.; Zhou, M.; Li, X. Spatiotemporally Controlled Multiplexed Photothermal Microfluidic Pumping under Monitoring of On-Chip Thermal Imaging. *ACS Sens.* **2019**, *4* (9), 2481−2490.
(12) Li, M.; Chen, T.; Gooding, J. J.; Liu, J. Review of Carbon and Graphene Quantum Dots for Sensing. *ACS Sens.* **2019**, *4* (7), 1732−1748.
(13) Quintanilla, M.; Liz-Marzán, L. M. Guiding Rules for Selecting a Nanothermometer. *Nano Today* **2018**, *19*, 126−145.
(14) Munro, T.; Liu, L.; Ban, H.; Glorieux, C. Thermophysical Properties of Thin Fibers via Photothermal Quantum Dot Fluorescence Spectral Shape-Based Thermometry. *Int. J. Heat Mass Transfer* **2017**, *112*, 1090−1097.
(15) Liu, L.; Zhong, K.; Munro, T.; Alvarado, S.; Côte, R.; Creten, S.; Fron, E.; Ban, H.; Van der Auweraer, M.; Roozen, N.; Matsuda, O.; Glorieux, C. Wideband Fluorescence-Based Thermometry by Neural Network Recognition: Photothermal Application with 10 Ns Time Resolution. *J. Appl. Phys.* **2015**, *118* (18), 184906.
(16) Foster, K. R.; Glaser, R. Thermal Mechanisms of Interaction of Radiofrequency Energy with Biological Systems with Relevance to Exposure Guidelines. *Health Phys.* **2007**, *92* (6), 609−620.
(17) Cerutti, G.; Prasad, R.; Farella, E. Convolutional Neural Network on Embedded Platform for People Presence Detection in Low Resolution Thermal Images. In ICASSP 2019 - 2019 IEEE International Conference on Acoustics, Speech and Signal Processing (ICASSP); 2019; pp 7610−7614.
(18) Lee, K.; Lee, J.; Lee, J.; Hwang, S.; Lee, S. Brightness-Based Convolutional Neural Network for Thermal Image Enhancement. *IEEE Access* **2017**, *5*, 26867−26879.
(19) Usamentiaga, R.; Molleda, J.; Garcia, D. F.; Granda, J. C.; Rendueles, J. L. Temperature Measurement of Molten Pig Iron With Slag Characterization and Detection Using Infrared Computer Vision. *IEEE Trans. Instrum. Meas.* **2012**, *61* (5), 1149−1159.
(20) Wang, N.; Li, Z.-L.; Tang, B.-H.; Zeng, F.; Li, C. Retrieval of Atmospheric and Land Surface Parameters from Satellite-Based Thermal Infrared Hyperspectral Data Using a Neural Network Technique. *International Journal of Remote Sensing* **2013**, *34* (9−10), 3485−3502.
(21) Ren, T.; Modest, M. F.; Fateev, A.; Sutton, G.; Zhao, W.; Rusu, F. Machine Learning Applied to Retrieval of Temperature and Concentration Distributions from Infrared Emission Measurements. *Appl. Energy* **2019**, *252*, 113448.
(22) Kim, S.; Kim, J.; Lee, J.; Ahn, J. Midwave FTIR-Based Remote Surface Temperature Estimation Using a Deep Convolutional Neural Network in a Dynamic Weather Environment. *Micromachines* **2018**, *9* (10), 495.
(23) Kim, Y.; Audigier, C.; Anas, E. M. A.; Ziegle, J.; Friebe, M.; Boctor, E. M. CUST: CNN for Ultrasound Thermal Image Reconstruction Using Sparse Time-of-Flight Information. In *Simulation, Image Processing, and Ultrasound Systems for Assisted Diagnosis and Navigation*; Stoyanov, D., Taylor, Z., Aylward, S., Tavares, J. M. R. S., Xiao, Y., Simpson, A., Martel, A., Maier-Hein, L., Li, S., Rivaz, H., Reinertsen, I., Chabanas, M., Farahani, K., Eds.; Lecture Notes in Computer Science; Springer International Publishing: Cham, 2018; pp 29−37.
(24) Pandit, S.; Banerjee, T.; Srivastava, I.; Nie, S.; Pan, D. Machine Learning-Assisted Array-Based Biomolecular Sensing Using Surface-Functionalized Carbon Dots. *ACS Sens.* **2019**, *4* (10), 2730−2737.
(25) Bisswanger, H. Enzyme Assays. *Perspectives in Science* **2014**, *1* (1), 41−55.
(26) Adzima, B. The Ember Printer: An Open Platform for Software, Hardware, and Materials Development. In Uv. eb West Conference, 2015.
(27) Gong, H.; Beauchamp, M.; Perry, S.; Woolley, A. T.; Nordin, G. P. Optical Approach to Resin Formulation for 3D Printed Microfluidics. *RSC Adv.* **2015**, *5* (129), 106621−106632.
(28) Sanchez, D.; Nordin, G.; Munro, T. Microfluidic Temperature Behavior in a Multi-Material 3D Printed Chip; ASME International

Mechanical Engineering Congress and Exposition; 2019; Vol. *10*: Micro-and Nano-Systems Engineering and Packaging.
(29) Zhou, C.; Zhao, W.; You, F.; Geng, Z.; Peng, H. Highly Stable and Luminescent Oxygen Nanosensor Based on Ruthenium-Containing Metallopolymer for Real-Time Imaging of Intracellular Oxygenation. *ACS Sens.* **2019**, *4* (4), 984−991.
(30) Phillips, D.; Drake, R. C.; O'Connor, D. V.; Christensen, R. L. Time Correlated Single-Photon Counting (Tcspc) Using Laser Excitation. *Instrum. Sci. Technol.* **1985**, *14* (3−4), 267−292.
(31) Lee, K. C. B.; Siegel, J.; Webb, S. E. D.; Lévêque-Fort, S.; Cole, M. J.; Jones, R.; Dowling, K.; Lever, M. J.; French, P. M. W. Application of the Stretched Exponential Function to Fluorescence Lifetime Imaging. *Biophys. J.* **2001**, *81* (3), 1265−1274.
(32) Roberts, A. J.; O'Connor, D. V.; Phillips, D. Multicomponent Fluorescence Decay in Vinyl Aromatic Polymers and Copolymers. *Ann. N. Y. Acad. Sci.* **1981**, *366* (1), 109−124.
(33) Gao, K.; Li, D. D.-U. Estimating Fluorescence Lifetimes Using Extended Kalman Filter. *Electron. Lett.* **2017**, *53* (15), 1027−1029.
(34) Munro, T.; Liu, L.; Glorieux, C.; Ban, H. CdSe/ZnS Quantum Dot Fluorescence Spectra Shape-Based Thermometry via Neural Network Reconstruction. *J. Appl. Phys.* **2016**, *119* (21), 214903.
(35) Wahl, M. Time-Correlated Single Photon Counting. *Technical Note* **2014**, 1−14.
(36) Sane, P.; Agrawal, R. Pixel Normalization from Numeric Data as Input to Neural Networks: For Machine Learning and Image Processing. In 2017 International Conference on Wireless Communications, Signal Processing and Networking (WiSPNET), 2017; pp 2221−2225.
(37) DeVries, T.; Taylor, G. W. Dataset Augmentation in Feature Space. ICLR 2017 conference, 2016.
(38) Mikolajczyk, A.; Grochowski, M. Data Augmentation for Improving Deep Learning in Image Classification Problem. In 2018 international interdisciplinary PhD workshop (IIPhDW), IEEE, 2018; pp 117−122.
(39) Stewart, M. Neural Network Optimization https://towardsdatascience.com/neural-network-optimization-7ca72d4db3e0 (accessed December 4, 2019).
(40) Géron, A. *Hands-On Machine Learning with Scikit-Learn, Keras, and TensorFlow: Concepts, Tools, and Techniques to Build Intelligent Systems*; O'Reilly Media: 2019.
(41) Ede, J. M.; Beanland, R. Adaptive Learning Rate Clipping Stabilizes Learning. arXiv preprint arXiv:1906.09060v2 [cs.LG], 2019.
(42) Kittel, C.; McEuen, P.; McEuen, P. *Introduction to Solid State Physics*; Wiley: New York, 1996; Vol. *8*.
(43) Varshni, Y. P. Temperature Dependence of the Energy Gap in Semiconductors. *Physica* **1967**, *34* (1), 149−154.
(44) Yakunin, S.; Benin, B. M.; Shynkarenko, Y.; Nazarenko, O.; Bodnarchuk, M. I.; Dirin, D. N.; Hofer, C.; Cattaneo, S.; Kovalenko, M. V. High-Resolution Remote Thermometry and Thermography Using Luminescent Low-Dimensional Tin-Halide Perovskites. *Nat. Mater.* **2019**, *18* (8), 846−852.
(45) Geitenbeek, R. Luminescence Thermometry: Fundamentals and Applications. PhD Thesis, Utrecht University, 2018.
(46) Eliseeva, S. V.; Bünzli, J.-C. G. Lanthanide Luminescence for Functional Materials and Bio-Sciences. *Chem. Soc. Rev.* **2010**, *39* (1), 189−227.
(47) R Bajgiran, K.; Darapaneni, P.; Melvin, A. T.; Dorman, J. A. Effects of Weak Electric Field on the Photoluminescence Behavior of Bi^{3+}-Doped YVO4:Eu^{3+} Core−Shell Nanoparticles. *J. Phys. Chem. C* **2019**, *123* (20), 13027−13035.
(48) Dong, H.; Sun, L.-D.; Feng, W.; Gu, Y.; Li, F.; Yan, C.-H. Versatile Spectral and Lifetime Multiplexing Nanoplatform with Excitation Orthogonalized Upconversion Luminescence. *ACS Nano* **2017**, *11* (3), 3289−3297.
(49) Gai, S.; Li, C.; Yang, P.; Lin, J. Recent Progress in Rare Earth Micro/Nanocrystals: Soft Chemical Synthesis, Luminescent Properties, and Biomedical Applications. *Chem. Rev.* **2014**, *114* (4), 2343−2389.
(50) Herrmann, M. G.; Durtschi, J. D.; Wittwer, C. T.; Voelkerding, K. V. Expanded Instrument Comparison of Amplicon DNA Melting Analysis for Mutation Scanning and Genotyping. *Clin. Chem.* **2007**, *53*, 1544.
(51) Seipp, M. T.; Durtschi, J. D.; Voelkerding, K. V.; Wittwer, C. T. Multiplex Amplicon Genotyping by High-Resolution Melting. *J. Biomol. Tech.* **2009**, *20* (3), 160.

https://dx.doi.org/10.1021/acsanm.0c00065
ACS Appl. Nano Mater. 2020, 3, 4045−4053